JOURNAL OF PROPULSION AND POWER
Vol. 11, No. 5, September–October 1995

Numerical Simulations of Flows in Centrifugal Turbomachinery

Daniel J. Dorney* and Roger L. Davis†
United Technologies Research Center, East Hartford, Connecticut 06108
and
Dennis K. McLaughlin‡
Pennsylvania State University, University Park, Pennsylvania 16802

A quasi-three-dimensional Navier–Stokes analysis has been extended and applied to flows in centrifugal turbomachinery blade rows. The numerical procedure was validated using a radial fan geometry typical of those found in fossil fuels plants and air-handling systems. The predicted blade loading and performance characteristics showed excellent agreement with the experimental data. The numerical analysis was then applied to a low AR centrifugal impeller. Inviscid and viscous flow simulations were performed at three operating conditions. While steady solutions were obtained in the inviscid flow calculations, the appearance of an oscillating separation bubble on the pressure surface of the impeller necessitated that the viscous flow simulations be time dependent. By comparing the predicted and experimental circumferential distributions of the relative frame velocity and flow angle downstream of the impeller, it was hypothesized that in the experiments the end-wall secondary flows energized the impeller suction surface boundary layer, making the flow locally behave like an inviscid fluid. The performance curve generated from the viscous calculations showed satisfactory agreement with the experimental data, while the inviscid calculations overpredicted the performance of the impeller. It was concluded that the physics retained in quasi-three-dimensional analysis give a useful first approximation of the flow trends in certain types of centrifugal turbomachinery.

Nomenclature

a = speed of sound
e_t = total energy
I = rothalpy
M = Mach number
P = static pressure
Pr = Prandtl number
q = total velocity
Re = freestream Reynolds number
r = radius
v, w = tangential and radial components of velocity
β = inlet, exit flow angle
θ = circumferential angle
κ = thermal conductivity
μ, λ = first and second coefficients of viscosity
ρ = density
τ = shear stress
Ω = rotational speed

Subscripts
i = inviscid
L = laminar quantity
N = normal direction
r, θ = first derivative with respect to r or θ
T = turbulent quantity
t = stagnation quantity
v = viscous
1/2 = inlet/exit quantity

Superscript
~ = relative frame quantity

Presented as Paper 93-2578 at the AIAA/SAE/ASME/ASEE 29th Joint Propulsion Conference, Monterey, CA, June 28–30, 1993; received Aug. 3, 1993; revision received Sept. 16, 1994; accepted for publication Sept. 21, 1994.

*Computational and Design Methods Group; currently Assistant Professor, Western Michigan University, Kalamazoo, MI. Member AIAA.

†Senior Principal Engineer, Computational and Design Methods Group. Member AIAA.

‡Department Chairman, Department of Aerospace Engineering. Member AIAA.

Introduction

CENTRIFUGAL compressor impellers are currently being used for a wide variety of applications such as gas turbine engines, air management systems, and rocket engine turbopumps due to their ability to compress air to relatively high pressure ratios over a short axial distance compared to axial compressors. The problem with these machines, however, is that they tend to be inefficient compared to their axial counterparts due to the relatively strong secondary flows that result from the radial turning of the flow and the rotational forces. The ability to accurately predict the flow characteristics of these impellers is essential for estimating and improving their aerodynamic performance in terms of losses and blade loading. Performance prediction for centrifugal compressors has previously relied heavily upon one-dimensional analytic techniques and two-dimensional potential flow solutions. While these inviscid, irrotational techniques may yield satisfactory predictions of midspan blade loading or overall stage efficiency, they cannot give information about the viscous, turbulent flow processes occurring within the impeller passage. It is these processes that control aerodynamic performance and are of the most interest to designers.

While two- and three-dimensional computational techniques for solving the turbulent Navier–Stokes equations are being increasingly used to analyze viscous flows within the blade passages of axial turbomachine compressors and turbines, much less effort has been put into developing similar techniques for centrifugal turbomachinery. One possible reason for the lack of prediction analyses available for centrifugal turbomachinery flows is that it is difficult to develop a numerical scheme that is capable of accurately resolving the many diverse flow phenomena that exist within the blade passages of these devices. Since most impeller blades are curved, swept, and twisted, grid generation becomes extremely dif-

ficult and can give rise to large truncation errors in the flow solution, even when a spatially high-order-accurate integration scheme is used. Truncation error can be especially troublesome, as it can overpower the natural dissipation mechanisms and can lead to inviscid (numerically induced) separation.[1] Among the researchers investigating full three-dimensional, computational techniques for centrifugal turbomachinery, Moore and Moore[2,3] and Rhie et al.[4] have developed partially parabolized Navier–Stokes procedures; Choi and Knight,[5] Dorney and Davis,[6] and Mounts et al.[7] solve the thin-layer Navier–Stokes equations; and Moore and Moore[8,9] and Hah et al.[10,11] solve the full Navier–Stokes equations. In general, these three-dimensional simulations are too expensive (computationally) to use the grid density required to resolve performance and boundary-layer quantities. Some researchers have applied two-dimensional numerical techniques to predict the flowfields within centrifugal and radial pumps. Miner et al.[12,13] and Badie et al.[14] have used two-dimensional potential flow techniques to predict the blade loadings and forces in centrifugal pump geometries. While the assumption of two-dimensional flow is computationally efficient, it ignores potentially important end-wall and stream-tube contraction effects. The two- and three-dimensional numerical investigations performed to date have increased the understanding of the flow structure within centrifugal turbomachinery blade passages, however, much more research is required to learn how to manipulate these flows to increase efficiency.

In this investigation, steady and unsteady flows in centrifugal turbomachinery are studied by extending the quasi-three-dimensional numerical analysis developed by Davis et al.[15,16] A quasi-three-dimensional procedure was chosen for this investigation because of the substantial savings in computer resources compared to full three-dimensional techniques, and the retention of important modeling physics such as stream-tube contraction. The information gained from the quasi-three-dimensional simulations can then provide guidance in future three-dimensional simulations by pinpointing regions of the flowfield where computational grid points should be concentrated, and furnishing the initial conditions for the flow variables. Thus, the goal of the current work is to determine if a quasi-three-dimensional flow procedure can be used to accurately predict, and increase the understanding of, the diverse flow phenomena present in centrifugal turbomachinery.

In the numerical analysis, known as RADFAN, the equations of motion are integrated using a spatially second-order-accurate, explicit, multiple-grid, finite volume, time-marching technique. The RADFAN procedure was chosen for this investigation because its flexible C-type computational grid topology eases the burden of grid generation for centrifugal geometries and because of the numerical algorithm's proven accuracy and efficiency, in both steady and time-dependent problems.[15,16] Validation of the RADFAN analysis was accomplished by performing inviscid and viscous simulations of the flow through the Wright radial fan,[17,18] and comparing the results to experimental data. To assess the ability of RADFAN to predict impeller performance at off-design flow conditions, numerical simulations were performed for the Worthington impeller[19] at three different operating conditions, and the predicted numerical results were compared with experimental data.

Physical Problem

The problem of interest in this investigation involves the steady and time-dependent flow through centrifugal and radial turbomachinery. The flow is assumed to be quasi-three-dimensional; i.e., the effects of radius change and stream-tube contraction are included in the mathematical modeling of the fluid dynamic equations. The assumptions used in deriving the quasi-three-dimensional equations of motion from the full three-dimensional Navier–Stokes equations result in certain limitations that must be considered when analyzing the predicted flowfield. In the present analysis, the flow at the computational inlet is assumed to consist of only radial and circumferential (tangential) components. In an actual radial impeller the inlet flow undoubtedly has an axial velocity component as well as recirculation zones caused by the abrupt change in the flow direction near the impeller backplate.

The quasi-three-dimensional effects in the numerical analysis are produced through stream-tube contraction, which models the "squeezing" of the flow due to the end-wall boundary layers. The stream-tube thickness, however, is varied only between the leading and trailing edges of the airfoil. This implies that the computational analysis is modeling an impeller that has a parallel-walled inlet section and a parallel-walled diffuser section. While the former condition is appropriate if the computational inlet is prescribed to be in the proximity of the airfoil leading edge, the latter condition may cause differences between the predicted numerical results and the experimental data if the actual machine does not have a parallel-walled diffuser.

The current procedure does not account for the secondary and reversed flows that are generated by the end walls of the turbomachine. Therefore, the predicted results of the numerical analysis should most closely resemble the experimental data near the midspan of the blade under consideration, and will be most accurate for blades that have a large AR. Fortunately, in most radial fans a significant portion of the flow near midspan is closely two dimensional in nature.[15] Even for flows in which three-dimensional effects are important in the midspan region, the pressure field is often only weakly coupled to the secondary flows, permitting the use of a quasi-three-dimensional procedure.

The effects of turbulence are modeled with an algebraic eddy viscosity correlation that has its basis in two-dimensional boundary-layer data, even though the actual flow in the blade passage may have reversed flow regions.[6] The choice of the current turbulence model, therefore, reflects a compromise between computational efficiency and numerical accuracy.

The main advantage of using a quasi-three-dimensional procedure is the substantial savings in computer resources compared to fully three-dimensional techniques. Fully three-dimensional unsteady simulations can require tens to hundreds of CPU hours on a Cray class supercomputer to achieve an engineering solution on a relatively coarse grid.[6,7] In addition, grid generation for complex three-dimensional geometries can require a trial-and-error process to produce a grid that yields a stable flow solution. Therefore, the simplification of the physics achieved by deriving the quasi-three-dimensional equations of motion allows the use of refined grids, and a more thorough investigation of the underlying physical mechanisms of centrifugal turbomachinery flows.

Mathematical Description

The governing equations of fluid motion considered in this study of centrifugal turbomachinery are the time-dependent, Reynolds-averaged, quasi-three-dimensional Navier–Stokes equations, which can be written in nondimensional form and cylindrical coordinates as

$$\frac{\partial \boldsymbol{Q}}{\partial t} + \frac{1}{r}\frac{\partial r(\boldsymbol{F}_i + Re^{-1}\boldsymbol{F}_v)}{\partial r} + \frac{1}{r}\frac{\partial(\boldsymbol{G}_i + Re^{-1}\boldsymbol{G}_v)}{\partial \theta} = S_{r\theta} \quad (1)$$

where the vector of conserved variables $\boldsymbol{Q}$, the inviscid flux vectors $\boldsymbol{F}_i$ and $\boldsymbol{G}_i$, the viscous flux vectors $\boldsymbol{F}_v$ and $\boldsymbol{G}_v$, and the source term $S_{r\theta}$, are given by

$$\boldsymbol{Q} = \begin{bmatrix} \rho \\ \rho v \\ \rho w \\ e_t \end{bmatrix} \qquad S_{r\theta} = \begin{bmatrix} 0 \\ -\rho w(v - 2\Omega r)/r \\ [P + \rho(v - \Omega r)^2]/r \\ 0 \end{bmatrix} \quad (2)$$

$$\boldsymbol{F}_i = \begin{bmatrix} \rho w \\ \rho v w \\ \rho w^2 + P \\ \rho w I \end{bmatrix} \qquad \boldsymbol{F}_v = -\begin{bmatrix} 0 \\ \tau_{r\theta} \\ \tau_{rr} \\ \tau_{hr} \end{bmatrix} \tag{3}$$

$$\boldsymbol{G}_i = \begin{bmatrix} \rho v \\ \rho v^2 + P \\ \rho v w \\ \rho v I \end{bmatrix} \qquad \boldsymbol{G}_v = -\begin{bmatrix} 0 \\ \tau_{\theta\theta} \\ \tau_{r\theta} \\ \tau_{h\theta} \end{bmatrix} \tag{4}$$

$$\tau_{rr} = 2\mu w_r + \lambda(w_r + v_\theta/r) \qquad \tau_{r\theta} = \mu(w_\theta/r + v_r)$$

$$\tau_{\theta\theta} = 2\mu v_\theta/r + \lambda(v_\theta/r + w_r)$$

$$\tau_{hr} = w\tau_{rr} + v\tau_{r\theta} + (\mu/Pr)(I_r - vv_r - ww_r)$$

$$\tau_{h\theta} = v\tau_{\theta\theta} + w\tau_{r\theta} + (\mu/rPr)(I_\theta - vv_\theta - ww_\theta)$$

$$e_t = \rho e + \rho[v^2 + w^2 - (\Omega r)^2]/2 \qquad I = (e_t + P)/\rho$$

Quasi-three-dimensional effects due to stream-tube contraction are included in the calculation of the control volume projected face areas.[16] The equations of motion are cast in blade-relative coordinates and, for the present application, the second coefficient of viscosity is calculated using Stokes' hypothesis, $\lambda = -\frac{2}{3}\mu$. The equations of motion are completed by the perfect gas law.

To extend the equations of motion to turbulent flows, an eddy viscosity formulation is used. Thus, the effective viscosity and effective thermal conductivity can be defined as

$$\mu = \mu_L + \mu_T \qquad \kappa/c_p = \mu_L/Pr_L + \mu_T/Pr_T \tag{5}$$

The turbulent viscosity μ_T is calculated using the two-layer Baldwin–Lomax[20] algebraic turbulence model. Although the validity of the Baldwin–Lomax model is suspect in flows with large separations, the model is very efficient and adequately gives the first-order effects of turbulence.

The theory of characteristics is used to determine the boundary conditions at the computational inlet and exit. For two-dimensional (or quasi-three-dimensional) problems, there are four characteristic waves that are associated with four eigenvalues. For subsonic inflow ($q_N < a$), three of the eigenvalues are positive and one is negative. This implies that at the inlet the characteristics corresponding to the three positive eigenvalues must be specified, while the characteristic corresponding to the negative eigenvalue is obtained from the solution algorithm used inside the computational domain. In this study, the total enthalpy h_t, the total pressure P_t, and the blade rotation speed Ω are used to represent the specified characteristics at the inlet. For subsonic outflow, the information associated with the three positive eigenvalues is transmitted to the boundary via the interior solution algorithm, while the information associated with the negative eigenvalue is specified. In this study, the average static pressure is used to represent the characteristic wave corresponding to the negative eigenvalue. Requiring that the average pressure across the exit boundary has a fixed value allows the local pressure to vary without affecting the mass flow rate.[16] This may also reduce the reflection of pressure waves as initial flow transients exit the computational domain.

No-slip boundary conditions are enforced along the airfoil surface for viscous flows, while flow tangency is enforced for inviscid flows. A periodicity condition is used along the wake centerline and at the outer boundary of the computational C-grid in the midgap region of the cascade passage. In the present study, the flow is assumed to be adiabatic.

Numerical Integration Procedure

An explicit, time-marching, control-volume, multiple-grid procedure is used to iteratively march the governing equations in time until a converged solution is obtained. The flow variables are updated in time according to a second-order-accurate Taylor series approximation and the distribution formulas developed by Ni.[21] A multiple-grid technique is used to accelerate the convergence rate for steady-state flow problems. The RADFAN numerical procedure uses C-type grids that are generated with an elliptic equation solution procedure, similar to that described in Ref. 22, to obtain a nearly orthogonal grid.

Wright Fan

A geometry chosen to validate the numerical procedure, RADFAN, is the forward-facing fan studied experimentally by Wright et al.[17,18] This fan is typical of those used in fossil-fuel powerplants and in industrial air-handling systems. The Wright fan provides an ideal test case for validating computational techniques, such as RADFAN, because detailed pressure measurements were taken along the surface of the blade. The fan, which has a diameter of 0.7620 m, was run at the design condition wheel speed of 125.7 rad/s. The span (hub-to-shroud distance) of the fan decreases from approximately 0.2540 m at the leading edge to 0.1905 m at the trailing edge. With a chord length of 0.2159 m, the AR of the blades is large enough to expect good agreement between the predicted results of the RADFAN analysis and the midspan experimental data. In the following discussions, the term "pressure surface" refers to the fan surface leading rotation, while the term "suction surface" refers to the surface trailing rotation.

To test the capabilities of the RADFAN analysis, both inviscid and viscous steady flow simulations were performed for the Wright fan test case. Performing both inviscid and viscous calculations is helpful in determining the effects of viscosity on fan performance. For the steady viscous flow simulation, the turbulent quantities were calculated only once every 20 iterations. In addition, two levels of multiple-grid acceleration and local time stepping were used in both the inviscid and viscous flow calculations. The calculations performed during this investigation were computed on an IBM RS-6000 workstation with 16 megabytes (MB) of memory. Typical inviscid computations required approximately 6000 iterations at 0.00015 s/grid point/iteration computation time to reach a converged solution. Typical viscous computations required approximately 10,000 iterations at 0.0006 s/grid point/iteration computation time to achieve a converged solution. In the following simulations, the static pressure at the computational exit was used to control the flow coefficient. In addition, the mass flow was held constant between the inviscid and viscous simulations by adjusting the exit static pressure.

A 597 × 17 (streamwise × tangential) computational grid was used to model one blade passage of the fan in the inviscid simulation. For the viscous simulation of flow through the Wright fan, a 597 × 33 computational grid was used to model one blade passage. Special attention was given to providing adequate leading and trailing-edge grid resolution, as these regions are important in determining viscous flow patterns.

Figure 1 illustrates the predicted and experimental surface pressure coefficient distributions for the Wright fan. The pressure coefficient is defined as

$$\hat{C}_P = \frac{2(P - P_1)}{\rho_1 (U_w)_{\text{tip}}^2} \tag{6}$$

where $(U_w)_{\text{tip}}$ is the fan tip velocity. The inviscid solution exhibits a slightly greater blade loading than the experimental data indicates, while the viscous solution shows excellent agreement with the experimental data. Although the inviscid and viscous simulations were performed at the same mass flow rate, the viscous simulation predicts a smaller blade loading because of boundary-layer blockage, which reduces the effective area of the fan passage. Streamlines contours can be very helpful in determining the global flow patterns within

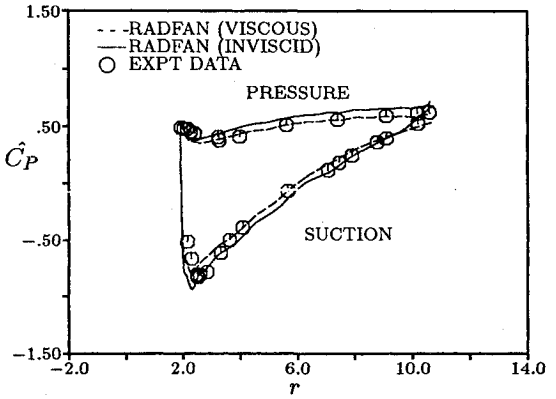

Fig. 1 Predicted and experimental pressure distributions for the Wright fan.

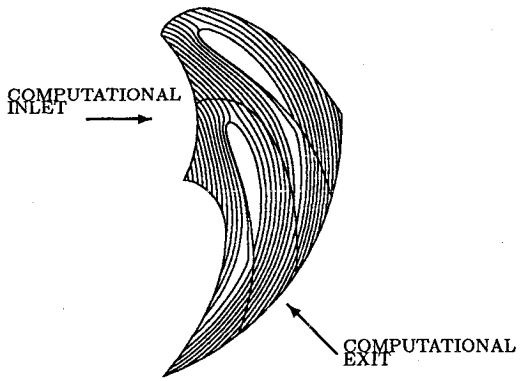

Fig. 2 Predicted streamline contours for the Wright fan, viscous simulation.

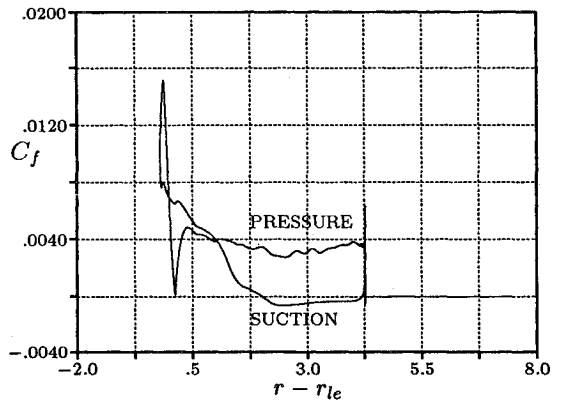

Fig. 3 Skin friction along the surface of the Wright fan.

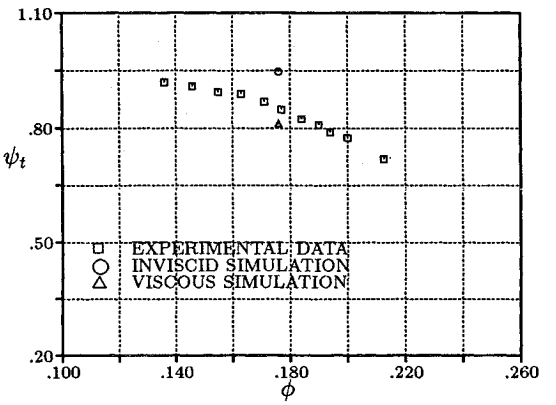

Fig. 4 Performance curve for the Wright fan.

the fan passage. Figure 2 illustrates the streamline contours for the viscous simulation. Near the suction surface trailing edge, the surface streamline moves away from the fan surface, possibly indicating the presence of a separation bubble. The skin friction coefficient C_f can be used to identify separated flow regions; a negative value of the skin friction signifies that the flow has separated. Figure 3, which shows the surface skin friction coefficient for one blade of the Wright fan, confirms that a shallow separation bubble exists from approximately 60% of the radial chord on the suction surface to the trailing edge. The performance of the fan was measured in the experimental tests by determining the variation of the total pressure coefficient as a function of the flow coefficient, where the total pressure rise coefficient is defined as

$$\psi_t = \frac{2(P_t - P_1)}{\rho_1 (U_w)^2_{\text{tip}}} \tag{7}$$

Figure 4 illustrates the predicted and experimental total pressure coefficients for the Wright fan. At the design flow coefficient of $\phi = 0.176$, the experimental value of the total pressure rise coefficient is approximately $\psi_t = 0.845$, the inviscid simulation produces a value of $\psi_t = 0.947$, and the viscous simulation yields $\psi_t = 0.812$. The difference between the total pressure rise in the inviscid and viscous simulations is mainly due to boundary-layer blockage and the separated flow region, which act to constrict the fan passage area and reduce the work done to the flow.

Worthington Impeller

The RADFAN computational procedure has also been used to perform "numerical experiments" for the Worthington impeller geometry (see Fig. 5).[19] Three sets of numerical simulations have been performed, one at the design and two at off-design flow operating conditions. Inviscid and viscous calculations were performed at all three operating conditions. The aerodynamic conditions used in the numerical simulations are presented in Table 1. Only the aerodynamic performance parameters from the $\phi = 0.12$ flow conditions are included

Table 1 Aerodynamic parameters for Worthington impeller

Parameter	$\phi = 0.06$	$\phi = 0.09$	$\phi = 0.12$
Q	0.1155 m³/s	0.1540	0.2310
Ω	314.15 rad/s	314.15	314.15
Re	1270.0/m	1270.0	1270.0
N	7	7	7
r_{1c}	0.0607 m	0.0607	0.0607
r_{1c}	0.1590 m	0.1590	0.1590

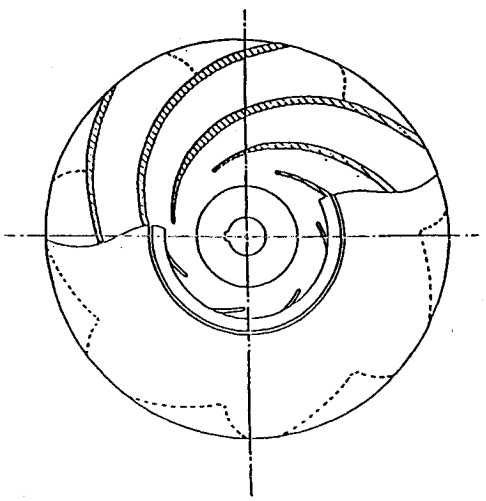

Fig. 5 Worthington impeller.[19]

in this study, as the other aerodynamic flow quantities at this flow coefficient are qualitatively similar to the $\phi = 0.09$ results.

Reference 19 presents experimental relative frame flow angle and velocity distributions for the first passage of the seven-bladed Worthington impeller. Experimental results were presented for only the first passage, since the flow in any blade passage was considered qualitatively representative of the flow in every blade passage. In the current study, however, the experimental data has been area averaged over the circumference of the impeller to facilitate comparison with the predicted results of the numerical simulations (which examines only one blade passage of the impeller). The surface definition of the Worthington impeller was obtained by discretizing an x-ray photograph of the impeller hub section (i.e., at the backplate). Since the Worthington impeller has swept blades and a constant airfoil section, the only difference between the hub section and the midspan section is the blade arc length. The errors associated with the manual discretization process cause the leading- and trailing-edge definition to differ slightly from that of the experimental impeller. In the numerical simulations, a circular arc was fit to the leading edge, while the trailing edge was generated at a constant radius. A 401 × 17 computational grid was used to model one blade passage of the impeller in the inviscid simulations. In the viscous simulations, a 641 × 25 computational grid was used to model one blade passage of the impeller.

Numerical experiments revealed that the viscous flow simulation produced a periodically oscillating, pressure surface, leading-edge separation bubble that precluded a steady-state solution. In addition, it was determined that this separation bubble gradually disappeared as the flow coefficient was reduced below the design point value. To preserve the fundamental physics of the viscous flow phenomena, the numerical analysis was used to perform time-dependent viscous flow simulations. Therefore, a global minimum time step was enforced, the turbulent quantities were calculated every iteration, and multiple-grid acceleration was not used. The frequency of the separation bubble oscillation was determined and the numerical results were time averaged over one period to facilitate comparison with the predicted results of the inviscid simulation and the experimental data. The period of one oscillation T_{osc} was determined to equal 4800 iterations. The period for one blade passing T_{bp} in the viscous calculations was 11,000 iterations. The Strouhal number can be defined as

$$St = f_{osc}/f_{bp} \tag{8}$$

where f_{osc} and f_{bp} are the separation bubble oscillation frequency and the blade passing frequency, respectively, and

$$f_{osc} = 2\pi/T_{osc} \tag{9}$$

$$f_{bp} = 2\pi/T_{bp} \tag{10}$$

The Strouhal number for the viscous design-flow simulation was calculated to be $St = 2.29$. This value is in the same range as that calculated from the experimental data,[19] and indicates that the quasi-three-dimensional analysis may be properly representing some of the flow physics associated with large-scale unsteadiness in this centrifugal impeller geometry.

Figure 6 illustrates the streamline pattern from the design flow viscous simulation, based on the time-averaged flowfield. The viscous results indicate a leading-edge separation bubble on the pressure surface of the impeller. The size of the separation bubble can be quantified by examining the time-averaged skin friction coefficient $\bar{C}_f$ along the surface of the impeller (see Fig. 7). The pressure surface separation bubble is large near the leading edge, then diminishes in size until the flow reattaches as it enters the uncovered portion of the

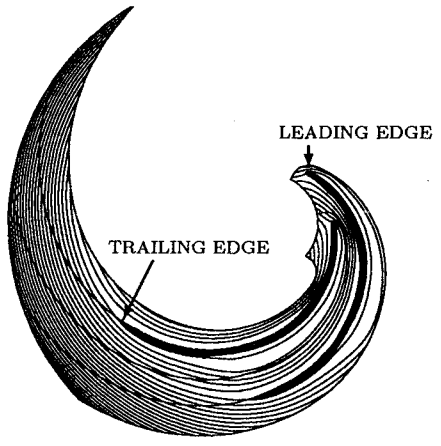

Fig. 6 Predicted streamlines for the Worthington impeller, viscous simulation, $\phi = 0.06$.

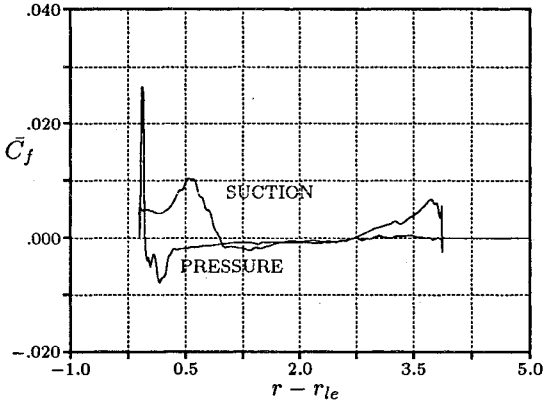

Fig. 7 Time-averaged skin friction along the surface of the Worthington impeller, $\phi = 0.06$.

passage. In addition, this figure reveals a shallow separation bubble on the suction surface of the blade, which extends from approximately 15% of the radial chord to the uncovered portion of the passage.

Figures 8 and 9 illustrate the blade-relative velocity ratio distributions from the experiment, the inviscid simulation, and the viscous simulation, respectively, at two different radii downstream of the trailing edge. These radii correspond to positions that are 1.875 and 5.000% greater than the trailing-edge radius of the impeller. In the current investigation, the velocity ratio is defined as the local relative velocity divided by the impeller tip velocity. All figures containing flow angle and velocity distributions have the trailing-edge location delineated by a solid vertical line, the pressure side of the passage denoted by PS, and the suction side of the passage denoted by SS. The experimental data[19] indicate a velocity jet near the trailing edge, which remains at approximately a constant circumferential location as a function of radius. As the flow in the jet moves downstream, it mixes with the surrounding fluid and gradually dissipates. The fact that the velocity jet is located on the pressure side of the trailing edge indicates that its presence may be, in part, due to the flow expanding around the constant radius portion of the trailing edge (similar to the Coanda effect). The velocity jet may also be associated with the jet-wake phenomena, as described by Eckardt.[23] The jet-wake phenomena is characterized by a pocket of high-momentum/high-velocity fluid collecting on the pressure side of the blade at the impeller exit (the jet), and a collection of low-momentum/low-velocity fluid developing near the suction side/shroud corner of the passage (the wake). In the midpassage region, the core flow is driven towards the pressure side of the passage at a relatively high velocity by a pair of counter-

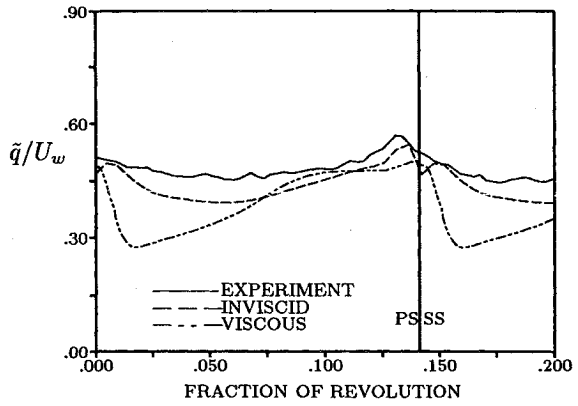

Fig. 8 Relative frame velocity magnitude for the Worthington impeller, $\phi = 0.06$, $\Delta R/R = 0.01875$.

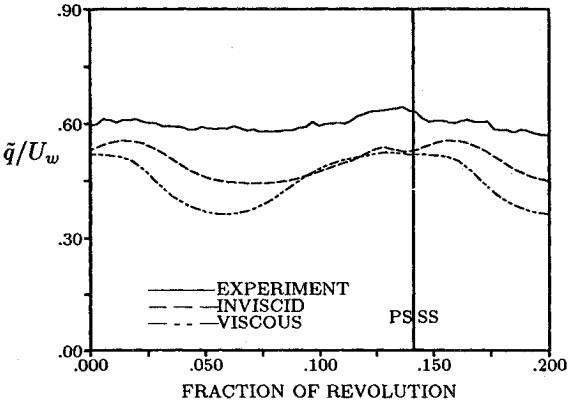

Fig. 9 Relative frame velocity magnitude for the Worthington impeller, $\phi = 0.06$, $\Delta R/R = 0.05000$.

rotating vortices. The spanwise location where the experimental data was acquired (approximately midspan) may correspond to this high velocity region between the two vortices. Thus, the assumption that the jet-wake phenomena is contributing to the velocity jet may explain why the jet remains at a constant circumferential location with increasing radius.

The predicted viscous results show a large velocity deficit in the suction side trailing-edge region. Downstream of the impeller passage, the wake mixes out and begins to lag behind the impeller rotation. The rapid circumferential movement of the viscous wake with increasing radius is due to the large tangential component of the velocity that develops as the flow moves along the constant radius portion of the trailing edge. The absence of a velocity jet in the viscous simulation is probably due to the absence of end-wall secondary flows in the numerical procedure. It is interesting that the predicted inviscid results do indicate a small jet in the trailing-edge region. This suggests that in the experiments the end-wall secondary flows energize the blade suction surface boundary layer, reducing the trailing-edge wake and making the flow appear locally inviscid. The inviscid velocity distribution matches very well with the experimental data near the trailing edge, but discrepancies become evident with increasing radius. These discrepancies correlate with differences in the flow-angle distributions and are probably caused by the lack of a diffuser in the experiment, and the lack of end-wall secondary flows and viscous effects in the inviscid numerical simulation. Although the inviscid and viscous flows exhibit different characteristics near the trailing edge, with the viscous results indicating a wake and the inviscid results showing a small jet, the two sets of numerical results show better agreement downstream of the trailing edge as the viscous wake mixes with the surrounding core flow.

Figures 10 and 11 illustrate the circumferential distributions of the blade-relative flow angle from the experiment, the inviscid simulation, and the viscous simulation, respectively, at the two radii discussed above. The inviscid simulation predicts relative flow angles that are nearly constant across the midpassage region, downstream of the impeller. The inviscid simulation also shows a flow angle deficit near the impeller trailing edge. The inviscid results indicate the flow is basically convected downstream of the trailing edge, except that a combination of numerical dissipation and truncation error smooths the trailing-edge flow angle deficit. Both the predicted viscous results and the experimental data indicate that the flow angle increases from the suction side of the passage to the pressure side of the passage. The results of the viscous simulation and the experimental data also show that the flow mixes out as it moves downstream, reducing the gradient in the flow angle associated with the trailing edge. Both the inviscid and viscous numerical results predict that the flow angle decreases more rapidly with radius than the experimental data indicates. One cause of this behavior is that in the experiment there was no diffuser section (i.e., the flow exited into free air), while the numerical procedure assumes that there is a parallel-walled diffuser. A second contributing factor is that the experimental flow angle distributions are undoubtedly affected by the end-wall secondary flows, which are not accounted for in the numerical procedure. In general, however, the flow angles predicted in the viscous simulation show good agreement with the experimental data. One conclusion that can be drawn from these numerical experiments is that a viscous simulation is necessary to predict the quantitative behavior of the flow angle (e.g., increasing flow angle from the suction side to the pressure side of the blade passage), while an inviscid simulation is probably sufficient for predicting the average flow angle.

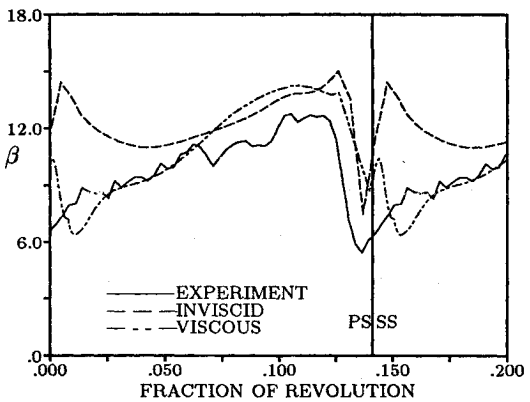

Fig. 10 Relative frame flow angle for the Worthington impeller, $\phi = 0.06$, $\Delta R/R = 0.01875$.

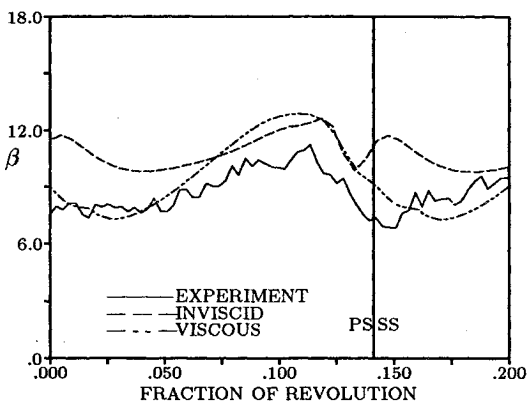

Fig. 11 Relative frame flow angle for the Worthington impeller, $\phi = 0.06$, $\Delta R/R = 0.05000$.

At the off-design operating conditions ($\phi = 0.09$), the blade loading predicted in the viscous simulation is much lower than that predicted at the design flow operating conditions. Investigation of the time-averaged results revealed that the average size of the temporally varying separation bubble was larger than that observed at the design flow conditions. The larger separation bubble causes increased blockage and reduces the useable work (pressure rise) available from the impeller for a given mass flow rate.

Figures 12 and 13 illustrate the blade-relative velocity ratio distributions from the experiment, the inviscid simulation, and the viscous simulation, respectively, at the same radii as above. At this flow coefficient ($\phi = 0.09$), the experimental data indicates that the velocity jet near the trailing edge has grown larger. The relative velocity within the jet varies very little with radius, implying that the absolute velocity is decreasing with increasing radius. This supports the hypothesis that the velocity jet may be caused by a combination of flow expansion around the trailing edge and secondary flows. At the higher flow coefficient the increased flow expansion creates a larger velocity jet, but the secondary flows become weaker and cannot sustain the jet. The results of the inviscid simulation also show that the velocity jet is somewhat larger than that predicted at the design flow conditions. The inviscid velocity distributions show very good agreement with the experimental data at both the radial locations, suggesting that as the end-wall secondary flows become weaker the flow in the midspan region of the impeller passage behaves more like a two-dimensional inviscid flow. The viscous results show a deeper wake than at the design flow conditions, as well as a more rapid increase in the velocity from the suction side of the passage to the pressure side of the passage. The viscous velocity distributions behave differently than the experimental data near the trailing edge, but exhibit improving agreement

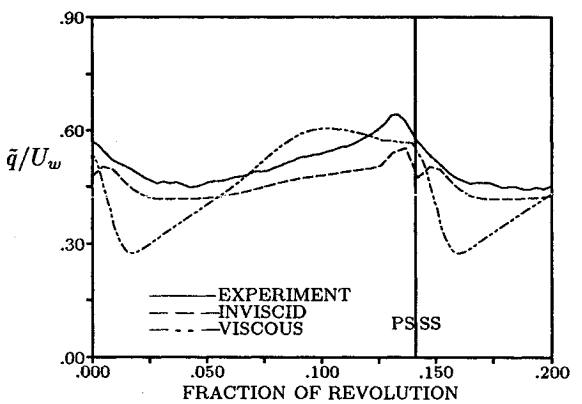

Fig. 12 Relative frame velocity magnitude for the Worthington impeller, $\phi = 0.09$, $\Delta R/R = 0.01875$.

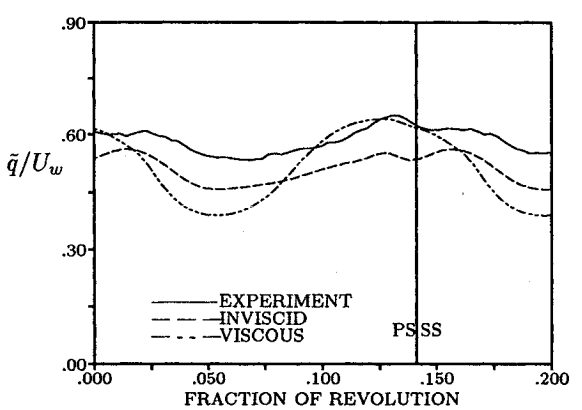

Fig. 13 Relative frame velocity magnitude for the Worthington impeller, $\phi = 0.09$, $\Delta R/R = 0.05000$.

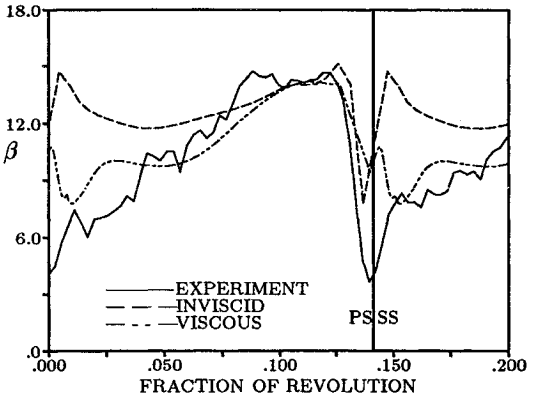

Fig. 14 Relative frame flow angle for the Worthington impeller, $\phi = 0.09$, $\Delta R/R = 0.01875$.

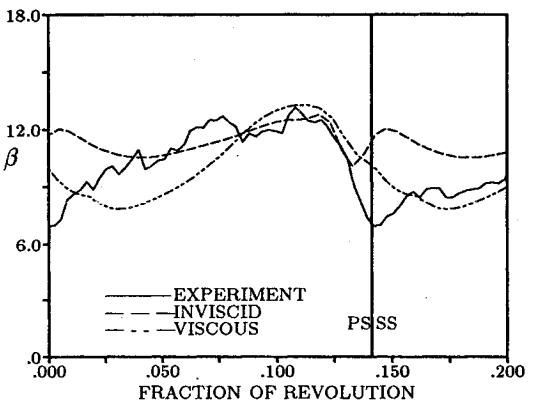

Fig. 15 Relative frame flow angle for the Worthington impeller, $\phi = 0.09$, $\Delta R/R = 0.05000$.

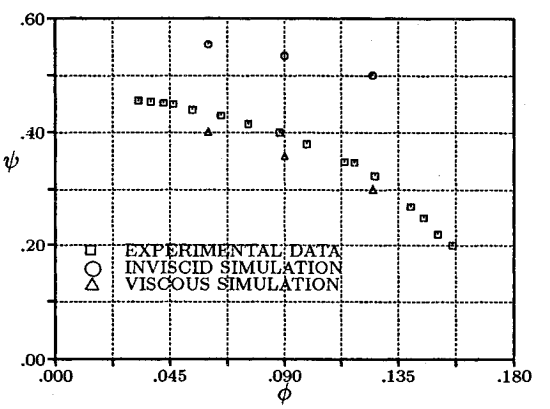

Fig. 16 Performance curve for the Worthington impeller.

with the experimental data farther downstream, as the wake mixes with the surrounding flow. All three data sets show greater velocity variations with radius in the midpassage region than in the proximity of the trailing edge.

Figures 14 and 15 illustrate the circumferential distributions of the blade-relative flow angle from the experiment, the inviscid simulation, and the viscous simulation, respectively, at the radii discussed previously and for a flow coefficient of $\phi = 0.09$. The relative flow angles from all three data sets have increased with the flow coefficient. The experimental flow angles show more variation with radius than was apparent at the design flow conditions. Again, this may signify that the secondary flows are not as strong as at the design flow coefficient, allowing the viscous effects to dissipate the velocity jet more rapidly. The flow angle distributions from the inviscid simulation show little variation across the blade passage and

a nearly linear decrease with radius. The inviscid flow angle distributions show only fair agreement with the experimental data near the trailing edge, but good agreement farther downstream after the jet-wake flow mixes with the surrounding core flow. The predicted viscous results indicate that the relative flow angle does not decrease as rapidly with radius as in the design flow calculation, which is in better agreement with the experimental data. As before, the viscous results and the experimental data show an increase in the relative flow angle from the suction side of the passage to the pressure side of the passage. In general, the flow angle distributions from the viscous simulation exhibit good agreement with the experimental data.

The aerodynamic performance of turbomachines is often quantified by measuring the variation of the static pressure rise coefficient with the variation in the flow coefficient, where the static pressure rise coefficient can be defined as

$$\psi = \frac{\Delta P}{\rho_1 (U_w)^2_{\text{tip}}} \tag{11}$$

Figure 16 illustrates the experimental and predicted pressure rise coefficient distributions for the Worthington impeller. At the design flow coefficient of $\phi = 0.06$, the experimental value of the pressure rise coefficient is approximately $\psi = 0.435$, the inviscid simulation yields a coefficient of $\psi = 0.551$, and the viscous simulation produces a value of $\psi = 0.401$. The predicted results of the inviscid simulation indicate a greater pressure rise through the impeller than either the experimental data or the viscous results due to the absence of separated flow or boundary-layer blockage. The pressure rise predicted by the viscous simulation agrees quite well with the experimental data. At a flow coefficient of $\phi = 0.09$, the experimental value of the pressure rise coefficient is approximately $\psi = 0.395$, the inviscid simulation gives $\psi = 0.529$, and the viscous simulation yields $\psi = 0.369$. Again, the inviscid simulation overpredicts the pressure rise, while the viscous results agree very well with the experimental data. Inviscid and viscous simulations were also performed at a flow coefficient of $\phi = 0.125$. At this flow coefficient, the experimental value of the pressure rise coefficient is approximately $\psi = 0.325$, the inviscid simulation gives $\psi = 0.490$, and the viscous simulation produces $\psi = 0.275$. Inspection of Fig. 16 reveals that the inviscid simulations consistently overpredict the pressure rise coefficient. This behavior is expected since the flow is subsonic (i.e., no shock losses), and there are no physical sources of loss in the inviscid procedure. The performance curve obtained from the viscous simulations more accurately represents the performance characteristics observed in the experiments. Thus, the inclusion of viscosity in the numerical modeling process is vital to the accurate prediction of aerodynamic performance. The favorable agreement between the viscous results and the experimental data also suggests that useful first approximations of the aerodynamic performance characteristics of certain radial turbomachinery geometries can be obtained without using expensive, fully three-dimensional numerical techniques.

Conclusions

A quasi-three-dimensional Navier–Stokes procedure has been modified and applied to steady and unsteady flows in centrifugal turbomachinery. The numerical analysis (RADFAN) was validated using the radial fan geometry of Wright.[17,18] Predicted blade loadings and performance parameters showed very good agreement with the experimental data.

The RADFAN procedure was used to perform "numerical experiments" for the Worthington impeller.[19] Inviscid and viscous flow calculations were performed at three different operating conditions. Relative frame flow angle and velocity ratio distributions predicted with the RADFAN analysis were compared with the experimental data at various locations downstream of the impeller trailing edge. While steady flow solutions were obtained in the inviscid calculations, the presence of an oscillating separation bubble in the viscous simulations required the solution of the time-dependent equations of motion. The time-averaged size of the separation bubble was observed to change as the flow coefficient was varied. The Strouhal number of the oscillation was in the same range as that determined experimentally. In general, the flow angle distributions obtained from the viscous simulations showed better agreement with the experimental data than the flow angles predicted in the inviscid simulations. Both the viscous simulations and experimental data indicated that the flow angle increased from the suction side of the blade passage to the pressure side of the blade passage. In the inviscid simulations, the flow angle remained relatively constant across the blade passage. The velocity distributions predicted in the inviscid simulations showed closer agreement with the experimental data than the velocity distributions obtained from the viscous simulations. The inviscid results and experimental data indicated a velocity jet near the trailing edge of the impeller, while the viscous simulations exhibited a wake in the trailing region. This suggests that in the experiments the end-wall secondary flows may energize the impeller suction surface boundary layer, making the flow locally behave like an inviscid fluid. The performance curve obtained from the viscous calculations showed close agreement with the experimental data. The inviscid simulations, as expected, overpredicted the performance of the impeller due to the lack of physical loss mechanisms (e.g., boundary layers, flow separation, etc.).

The favorable agreement between the numerical results and the experimental data suggests that quasi-three-dimensional flow procedures may be used to gain an understanding of the flow mechanisms in certain centrifugal turbomachines.

References

[1]Eriksson, L.-E., "Simulation of Transonic Flow in Radial Compressors," *Computer Methods in Applied Mechanics and Engineering*, Vol. 64, 1987, pp. 95–111.

[2]Moore, J., and Moore, J. G., "Calculation of Three-Dimensional Viscous Flow and Wake Development in a Centrifugal Impeller," *Performance Prediction of Centrifugal Pumps and Compressors*, American Society of Mechanical Engineers, New York, 1979.

[3]Moore, J., and Moore, J. G., "Three-Dimensional Viscous Flow Calculation for Assessing the Thermodynamic Performance of Centrifugal Compressors, Study of the Eckardt Compressor," *Proceedings of the AGARD Meeting on Centrifugal Compressors, Flow Phenomena and Performance* (Brussels, Belgium), No. 282, 1980.

[4]Rhie, C. M., Delaney, R. A., and Mckain, T. F., "Three-Dimensional Viscous Flow Analysis Centrifugal Impellers," AIAA Paper 84-1296, June 1984.

[5]Choi, D., and Knight, C. J., "Computations of 3D Viscous Flows in Rotating Turbomachinery Blades," AIAA Paper 89-0323, 1989.

[6]Dorney, D. J., and Davis, R. L., "Centrifugal Compressor Impeller Aerodynamics (A Numerical Investigation)," American Society of Mechanical Engineers, ASME Paper 90-GT-213, June 1990.

[7]Mounts, J. S., Dorney, D. J., and Brasz, J. J., "Flowfield Analysis of a Backswept Centrifugal Impeller," AIAA Paper 91-2470, June 1991.

[8]Moore, J., and Moore, J. G., "3-D Viscous Flow Calculations at Design and Off-Design Conditions for the NACA 48-Inch Radial-Inlet Centrifugal Impeller," *Proceedings of the 8th International Symposium on Air Breathing Engines*, 1987, pp. 139–148.

[9]Moore, J., and Moore, J. G., "Secondary Flow, Separation and Losses in the NACA 48-Inch Centrifugal Impeller at Design and Off-Design Conditions," American Society of Mechanical Engineers, ASME Paper 88-GT-101, June 1988.

[10]Hah, C., Bryans, A. C., Moussa, Z., and Tomsho, M. E., "Application of Viscous Flow Computations for the Aerodynamic Performance of a Back-Swept Impeller at Various Operating Conditions," American Society of Mechanical Engineers, ASME Paper 88-GT-39, June 1988.

[11]Hah, C., and Krain, H., "Secondary Flows and Vortex Motion in a High Efficiency Backswept Impeller at Design and Off-Design Conditions," American Society of Mechanical Engineers, ASME Pa-

per 89-GT-181, June 1989.

[12]Miner, S. M., Flack, R. D., and Allaire, P. E., "Two-Dimensional Flow Analysis of a Laboratory Centrifugal Pump," American Society of Mechanical Engineers, ASME Paper 90-GT-50, June 1990.

[13]Miner, S. M., Flack, R. D., and Trevisan, P., "Potential Flow Analysis of the Forces on a Laboratory Centrifugal Pump Impeller," American Society of Mechanical Engineers, ASME Paper 92-GT-285, June 1992.

[14]Badie, R., Jonker, J. B., and Van Essen, T. G., "Calculations on the Time-Dependent Potential Flow in a Centrifugal Pump," American Society of Mechanical Engineers, ASME Paper 92-GT-151, June 1992.

[15]Davis, R. L., "Prediction of Viscous Flows in Rotating Machinery Using Navier-Stokes Techniques," 3rd International Symposium on Transport Phenomena and Dynamics of Rotating Machinery, Honolulu, HI, April 1990.

[16]Davis, R. L., Ni, R. H., and Carter, J. E., "Cascade Flow Analysis Using the Navier-Stokes Equations," *Journal of Propulsion and Power*, Vol. 3, No. 5, 1987, pp. 406–414.

[17]Wright, T., "Centrifugal Fan Performance with Inlet Clearance," *Journal of Engineering for Gas Turbines and Power*, Vol. 106, Oct. 1984, pp. 906–912.

[18]Wright, T., Tzou, K. T. S., Greaves, K. W., and Madhavan, S., "The Internal Flow Field and Overall Performance of a Centrifugal Fan Impeller—Experiment and Prediction," American Society of Mechanical Engineers, ASME Paper 82-JPGC-GT-16, 1982.

[19]Choi, J. S., "Experiments on the Unsteady Flowfield Associated with Noise Generation in Centrifugal Turbomachinery," Ph.D. Dissertation, Pennsylvania State Univ., University Park, PA, Dec. 1991.

[20]Baldwin, B. S., and Lomax, H., "Thin-Layer Approximation and Algebraic Model for Separated Turbulent Flows," AIAA Paper 78-257, Jan. 1978.

[21]Ni, R. H., "A Multiple-Grid Scheme for Solving the Euler Equations," *AIAA Journal*, Vol. 20, No. 11, 1982, pp. 1565–1571.

[22]Sorenson, R. L., "A Computer Program to Generate Two-Dimensional Grids About Airfoils and Other Shapes by the Use of Poisson's Equation," NASA TM-81198, May 1980.

[23]Eckardt, D., "Instantaneous Measurements in the Jet-Wake Discharge Flow of a Centrifugal Compressor Impeller," *Journal of Engineering for Power*, Vol. 97, No. 3, 1975, pp. 337–346.